

Multiple Abnormality Detection for Automatic Medical Image Diagnosis Using Bifurcated Convolutional Neural Network

M. Hajabdollahi, R. Esfandiarpour, E. Sabeti, N. Karimi, K. Najarian,,
S.M.R. Soroushmehr, S. Samavi

Abstract— Automating classification and segmentation process of abnormal regions in different body organs has a crucial role in most of medical imaging applications such as funduscopy, endoscopy, and dermoscopy. Detecting multiple abnormalities in each type of images is necessary for better and more accurate diagnosis procedure and medical decisions. In recent years portable medical imaging devices such as capsule endoscopy and digital dermatoscope have been introduced and made the diagnosis procedure easier and more efficient. However, these portable devices have constrained power resources and limited computational capability. To address this problem, we propose a bifurcated structure for convolutional neural networks performing both classification and segmentation of multiple abnormalities simultaneously. The proposed network is first trained by each abnormality separately. Then the network is trained using all abnormalities. In order to reduce the computational complexity, the network is redesigned to share some features which are common among all abnormalities. Later, these shared features are used in different settings (directions) to segment and classify the abnormal region of the image. Finally, results of the classification and segmentation directions are fused to obtain the classified segmentation map. Proposed framework is simulated using four frequent gastrointestinal abnormalities as well as three dermoscopic lesions and for evaluation of the proposed framework the results are compared with the corresponding ground truth map. Properties of the bifurcated network like low complexity and resource sharing make it suitable to be implemented as a part of portable medical imaging devices.

Index Terms—Convolutional neural network; wireless capsule endoscopy; skin cancer, multiple abnormality detection, structural complexity, hardware implementation.

I. INTRODUCTION

Automatic segmentation and classification of abnormalities in different body organs has become very important in medical imaging applications. In different medical imaging applications such as endoscopic, dermoscopic, and fundoscopic imaging, automatic segmentation and classification of abnormalities greatly help physicians in the diagnosis process. Automatic medical image processing also reduces the time spent by medical experts for analysis of images and video frames. Classification and segmentation are utilized by medical imaging applications to detect single or multiple abnormalities. In the scope of single abnormality detection, there are different types of abnormalities which are required to be detected automatically. Different abnormalities in *wireless capsule endoscopy* (WCE), fundoscopic images, and different lesions in dermoscopic images are examples of multiple abnormalities which are extensively studied to be automatically detected. WCE, a non-invasive modality for remotely screening all parts of human's *gastrointestinal* (GI) system, can be used in detecting different types of abnormalities such as bleeding and Crohn's disease [1]. Since the emergence of the capsule endoscopy device in 2001 [2], there have been many efforts for automatic detection of different abnormalities in WCE images. The goal of these efforts was to shorten the screening time spent by physicians and increasing the accuracy of diagnosis. Automatic detection of abnormalities in WCE images has been investigated as multiple or single abnormality detection problems [3].

In case of single abnormality detection in WCE, in [3], a *convolutional neural network* (CNN) architecture is used for classification of bleeding images. In [4], features extracted by CNN as well as features from K-means clustering are used for classification of bleeding images. Vieira *et al.* in [5], invented an accelerated expectation maximization method named maximum posterior to classify images into angiodysplasia and other abnormalities. Also, Markov random field is used to take spatial information into account. Fu *et al.* in [6], proposed a method for bleeding regions detection in WCE images. In their work, after removing detected edge pixels, superpixels are created by a grouping approach. Finally, superpixels are classified by SVM. In [7], initial seeds detected using K-

Mohsen Hajabdollahi, Reza Esfandiarpour, and Nader Karimi are with the Department of Electrical and Computer Engineering, Isfahan University of Technology, Isfahan 84156-83111, Iran.

E. Sabeti is with the Department of Computational Medicine and Bioinformatics, University of Michigan, Ann Arbor, U.S.A.

S.M. Reza Soroushmehr is with the Michigan Center for Integrative Research in Critical Care, and also with the Department of Computational Medicine and Bioinformatics, University of Michigan, Ann Arbor, U.S.A.

Kayvan Najarian is with the Department of Computational Medicine and Bioinformatics; Department of Emergency Medicine; and the Michigan Center for Integrative Research in Critical Care, University of Michigan, Ann Arbor, U.S.A.

Shadrokh Samavi is with the Department of Electrical and Computer Engineering, Isfahan University of Technology, Isfahan 84156-83111, Iran. He is also with the Department of Emergency Medicine, University of Michigan, Ann Arbor, U.S.A.

means are labeled by *support vector machine* (SVM), then bleeding regions are segmented using an interactive segmentation based on cellular automata. In [8], WCE images are represented using local binary pattern and average saturation and are classified using SVM in bleeding and non-bleeding regions. In [9], color information of selected points by SURF are extracted and classified as lesion and non-lesion regions. In this study different types of abnormalities are considered as one class and healthy parts as the other one.

Since there are different types of abnormalities in GI, the problem of detecting multiple abnormalities is addressed in a number of studies. Seguí *et al.* in [10], designed a CNN for detection of different GI events such as bubbles, wrinkles, and others. Yuan *et al.* in [11], utilized an SVM for classifying polyps, ulcer, and other abnormalities using three main features extracted from the original image. These features include color and texture features clustered by K-means, saliency map obtained through color and texture, and local manifold structure resulted from nearest neighbor graph. A single CNN structure is used by [12] for classification of body organs including stomach, small intestine, and colon. Iakovidis *et al.* in [13], detected bleeding regions by defining a criteria on super pixel saliency. In [14], a robust modified speeded-up feature is used to include color features which are important in WCE images. Then SVM is used for classification of abnormal and normal images. A single CNN structure is used as a binary classifier for detection of different abnormalities separately by Sekuboyina *et al.* in [15]. Deeba *et al.* in [16], detected salient regions using conditional probability of a region around each pixel and also identified different types of abnormalities using adaptive thresholding. Vasilakakis *et al.* in [17], took advantage of clustering algorithms and SURF to extract a bag of visual words. Finally, a trained SVM is applied to detect inflammatory lesions. In [18], semantic information of WCE images is used for better lesion classification. The difference of maximum points is used as a bag of words for salient point detection, and in order to detect different objects in WCE images, multi-label classification is used.

Malignant skin lesion is almost the most common type of cancer worldwide. In the scope of automatic diagnosis of various lesions in dermoscopic images, melanoma and non-melanoma images should be discriminated properly. Dermoscopy can be used to discriminate between benign and malignant skin lesions also diagnostic capability can be improved [19]. Problem of automatic lesion detection in dermoscopic images has been investigated to discriminate between melanocytic and non-melanocytic lesions. In [20] an automatic system for detection of pigment network is designed and results are used for diagnosing melanoma lesions. To this end, pigment network is extracted based on 2-D Gabor filtering and also more features are extracted based on color, texture and geometric properties. At last, a neural network and an SVM are applied to classify images as benign and malignant based on aforementioned features. Ruela *et al.* in [21], in order to detect melanomas, selected the best shape and symmetry descriptors by analyzing a variety of descriptor's properties. In their work, dermoscopic images are segmented and a subset of features is extracted using a filter approach method. Finally, images were classified as melanoma and non-

melanoma using KNN classifier. To classify skin lesions, Nasir *et al.* in [22], after hair removal and contrast enhancement steps, extracted abnormal regions of the image using active contour and uniform distribution based segmentation. In their work, in the segmented area, color and texture features are extracted and classified using SVM classifier. In [23], considering that *Fourier transform* (FT) is able to extract different image patterns, main frequencies of FT are used as input features for classification of melanoma. Co-occurrence matrix is created using main frequencies of FT and then images are classified by applying a *multi-layer perceptron* (MLP) and SVM. In [24], skin lesions are segmented using fully convolutional neural network. Data imbalance problem between normal and abnormal regions is alleviated by defining a loss function that takes imbalance data problem into account for better segmentation. In [25], a multi-stage fully convolutional neural network is proposed to segment abnormal regions of dermoscopic images. In the first stage, a fully convolutional neural network conducts the segmentation task based on input image and in the next stages, segmentation is performed using estimated segmentation map resulted from the previous stage. In [26], lesion analysis is conducted using different image labeling. Skin lesions are segmented to different regions based on their color and texture using a graph based method. Each segmented region is represented using color and texture features and labeled using a method named corr-LDA. After that lesion is classified using various classifiers including random forest, KNN, and SVM. In [27], a skin lesion segmentation method is proposed. Hairs in skin images are removed and region of interest is segmented using region growing approach. In [28], after segmentation of lesion, 2-D and 3-D representation of images are reconstructed. Then classification is performed using different features including shapes of 2-D and 3-D reconstruction as well as texture and color. In [29], skin lesions are labeled with concentration on the border of lesions. After using an active contour method for segmentation, local features are extracted from the border of the lesion and other features are extracted from inside of the segmented area. Finally lesions are labeled by an SVM. In [30] an automatic lesion segmentation in dermoscopic images is presented. Skin areas are detected using a thresholding method and lesion regions are segmented using a Delaunay triangulation method. Final segmentation map is obtained by fusing results of lesion segmentation and skin detection step.

Developing a battery operated handheld device with capability of automatic segmentation and classification of medical abnormalities is very demanding [31]. Development of methods for skin cancer screening using devices such as smartphones and portable cameras for skin screening, has provided efficient diagnosis services at a very low cost. Simple and efficient diagnosis procedures should be designed for use in portable devices which are small and limited in battery life-time. In [32] and [33] a lightweight method for melanoma detection in smartphones is developed. Also in [34], a device for automatic real-time screening of skin is designed to classify region of interest as benign and malignant. In [35] a handheld system for automated detection of melanoma is designed. In [36] a hardware

system for analysis of skin lesions is proposed and implemented on an embedded platform.

Also in WCE image analysis, a number of researchers have investigated the problem of energy consumption and designed several simple and low power structures for all parts of the capsule. Detecting keyframes inside the capsule and only transmitting important frames could effectively reduce the amount of energy consumed by the capsule. In this regard, in [37], a technique to summarize WCE video frames is proposed. The keyframes are detected using moments, curvature, and image's contrast information and other frames are dropped. In [38], a method for frame saliency detection based on some different moments is proposed and implemented on FPGA. In [39], bleeding regions are detected using an *artificial neural network* (ANN) structure. The network structure is simplified to become suitable for hardware implementation inside the capsule.

In the endoscopy process conducted by a capsule, images should be transmitted outside the capsule. Hence, compression is introduced as a proper way to reduce the amount of transmitted data [40]. In [41], an FPGA implementation of data processing core with a focus on image compression for WCE device is presented. In [42], a low complexity architecture for one-dimensional *discrete cosine transform* (DCT) transform is presented. Using Cordic-Loeffler technique, the DCT transform has become suitable for compression inside the capsule. In [43], concerning low-resolution and properties of WCE images, specific patterns in different channels of image are extracted for DPCM coding and are utilized for better compression.

In the scope of implementing automatic medical image processing methods inside portable devices, there are two main problems. First, a few research studies have investigated the problem of detecting multiple abnormalities inside the portable medical devices such as digital dermatoscope and WCE device. Second, there is no simple and efficient CNN structure for simultaneous segmentation and classification of multiple abnormalities. Solving these problems can be very beneficial for better and easier diagnosis in medical portable device.

To address the aforementioned problems, in this paper, a new algorithm for segmentation and classification of various abnormalities in different medical applications is presented. The proposed bifurcated neural network segments the images in one direction and classifies them in the other direction.

Thanks to existence of common low-level features in all abnormalities, main part of the proposed network is designed to be the same in both directions. The network is designed to have a simple structure and share computational operations. The contribution of the proposed method can be regarded as follows:

- Design a simple network structure for both segmentation and classification of different abnormalities in medical images.
- Design a bifurcated network with a shared primary part extracting common features which are useful for both segmentation and classification of different abnormalities.
- Resource reusability in the primary part of the proposed network leading to a simple network with low structural complexity suitable for portable medical devices.

The remainder of this paper is organized as follows. In Section II, different structures for classification of multiple abnormalities are presented. In Section III, the proposed bifurcated network for detection of multiple abnormalities is presented. Section IV is dedicated to experimental results, and finally, in Section V the concluding remarks are presented.

II. MULTIPLE ABNORMALITY DETECTION

Classification and segmentation of multiple abnormalities are used in many medical applications such as endoscopic, dermoscopic, funduscopy, etc. Abnormalities such as microaneurysms and exudate in retinal images and bleeding, ulcer and chylous in GI images are examples of multiple abnormalities related to important diseases. In recent years CNN has become very popular for efficient automatic detection of abnormalities in medical imaging applications. Multiple abnormalities can be detected using different CNN structures which are briefly explained as follows.

A. Single network structure for multiple abnormality detection

A straightforward solution for multiple abnormality detection is utilizing a single structure for all types of abnormalities. In Fig. 1, a sample patch-based CNN structure for abnormality detection in endoscopic images is illustrated. In this structure, the network is trained using all types of

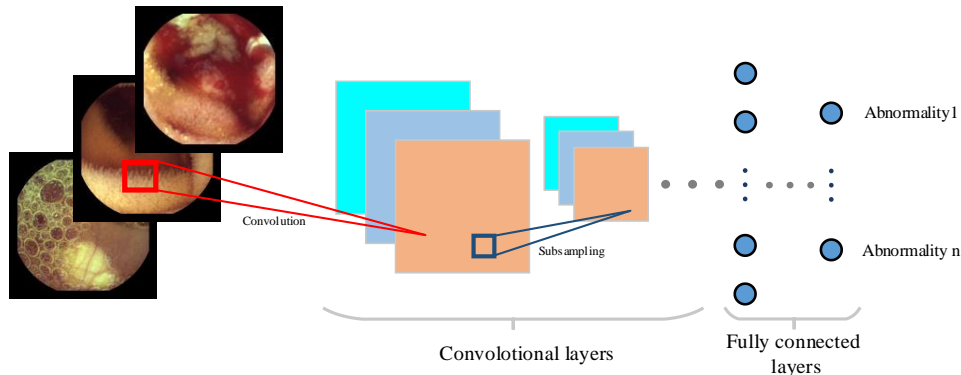


Fig. 1. Single CNN structure for multiple abnormality detection

abnormalities and classifies an input pixel into one of the abnormality classes according to its surrounding patch. In Fig. 1, Classification is performed based on the surrounding patch of each pixel, and this classification can be utilized for classification and segmentation of the whole image. Single structure of neural network has been used in recent years to detect body organs and abnormalities. As mentioned earlier, in [10, 12, 15], the problem of classification of WCE images was addressed. Also classification of multiple abnormalities is investigated in other areas such as retinal image analysis [26-27]. In [44], a single CNN structure is used for segmentation of optic disk, fovea, and blood vessels. In [45], a single CNN structure is utilized for segmentation of exudates, bleeding, and micro-aneurysms. Although a single structure is utilized in many research areas, but the resulting network tends to be computationally complex. For example in [3] and [10], about 15×10^6 and 2.2×10^6 paramet are utilized, respectively. Having so many parameters is troublesome for implementation of an algorithm inside a portable medical device. Also during training the single network structure, each abnormality modifies the whole network variables which can cause poor classification performance in case of abnormalities with much variation.

Designing a simple and adequately accurate CNN structure for detecting multiple abnormalities inside portable devices is a challenging task. Moreover, in some situations, abnormalities are very different in color, size, and feature. Hence, it is not possible to utilize an efficient single structure for detecting all types of abnormalities. Assigning special parts of the network to each abnormality can be regarded as an efficient way for better training the network. In this manner, each part of the network is trained and customized for a special abnormality and could be exclusively improved and optimized.

B. Separate network structure dedicated to each abnormality

In Fig. 2, separate networks are dedicated to each abnormality. As illustrated in Fig. 2, each network is trained using only one abnormality image dataset. Each network can accurately segment the abnormality used during the training phase. In this manner, each network structure is better specialized and customized on an individual abnormality, but it is not able to indicate the abnormality class. In these networks, there is no cooperation among elements of separate networks and similar features among abnormalities are not utilized which increases the overall complexity of the network structure. Although these networks are specialized adequately, they suffer from redundant operations. Furthermore, they are only useful for segmentation and do not help in the classification task. Concerning multiple abnormality segmentation and classification, there must be a possibility to concentrate on each abnormality as needed for segmentation without loss of generality required for classification.

III. PROPOSED BIFURCATED NETWORK FOR ABNORMALITY CLASSIFICATION AND SEGMENTATION

In Fig. 3, two different abnormalities in WCE and dermoscopic images are depicted with their corresponding ground truth, respectively. There are various abnormalities that are common in human GI and skin which can be related to important diseases. Abnormal regions are different in color, texture and other features. For better diagnosis capability, both segmentation and classification of abnormal regions are required. Single network structure is not specialized for individual abnormalities. Hence, it is not always possible to appropriately train the network to reach a proper performance. Moreover, separate networks for each abnormality are not able to classify the images into abnormality classes and suffer from

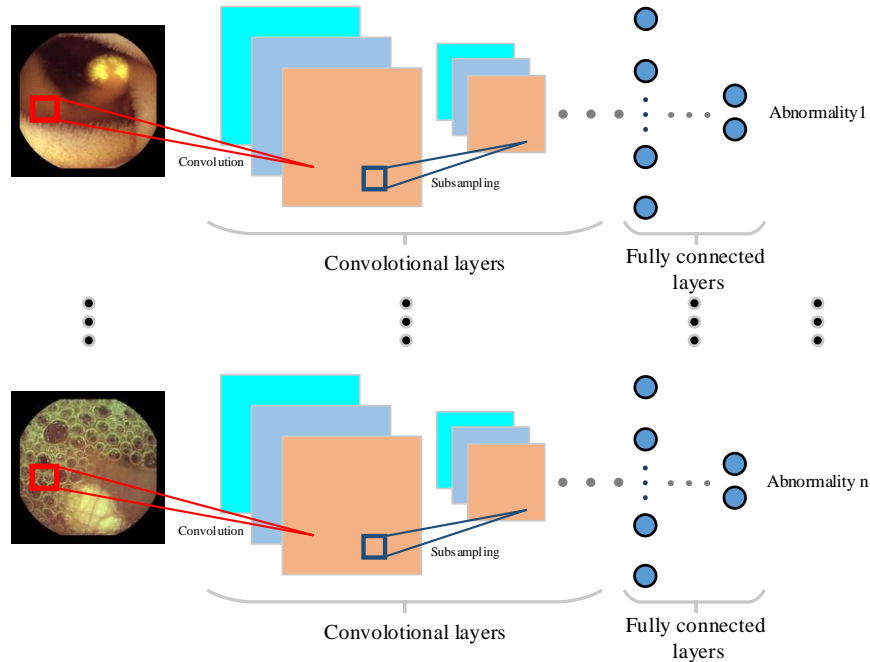


Fig. 2. Separate networks dedicated to each abnormality.

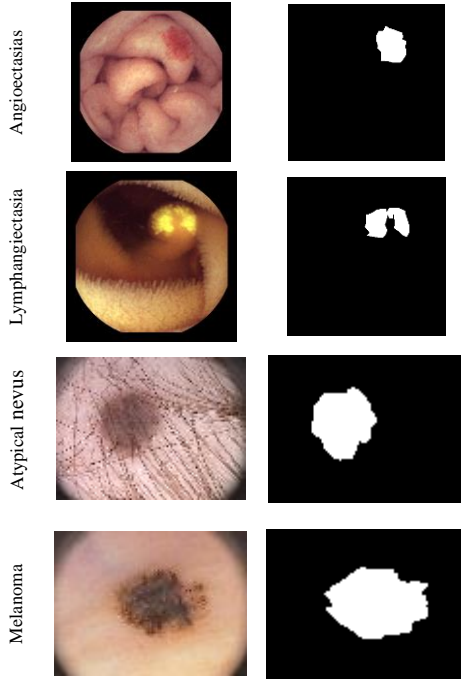


Fig. 3. Four examples of abnormalities in endoscopic and dermoscopic images and corresponding Ground Truth

redundant operations. In the following subsections, the proposed network addresses these problems.

A. Overview of the proposed framework

In Fig. 4, a general block diagram of the proposed framework is shown. We first train separate neural networks where each one is dedicated to a specific abnormality and can segment that abnormality precisely. Then, the first parts of all trained segmentation networks are merged to make the primary part of the final network. The principal idea here is that when the primary parts of the several neural networks are merged, the secondary parts are needed to be retrained exclusively to retain the same functionality as before. Let's talk about this claim in more detail for a simple example of n different 3-layer MLP networks. A neural network in general can be interpreted as a type of Markov random field, with a layer of neurons as a vector of stochastic visible (input) unit \mathbf{v} and vectors of various stochastic hidden units \mathbf{h} . In our example of Fig. 5, suppose each network is trained on a specific class of input, results in n different sets of weight matrices $\mathcal{W}^1, \mathcal{W}^2, \dots, \mathcal{W}^n$, where $\mathcal{W}^i = \{W_1^i, W_2^i, W_3^i\}$ is the set of weight matrices of 3 layers trained on i th input class (abnormality). In this setup, the outputs of networks are

$$\begin{cases} \mathbf{y}^1 = \mathbf{h}_3^1 = W_3^1 W_2^1 W_1^1 \mathbf{v}^1 \\ \mathbf{y}^2 = \mathbf{h}_3^2 = W_3^2 W_2^2 W_1^2 \mathbf{v}^2 \\ \vdots \\ \mathbf{y}^n = \mathbf{h}_3^n = W_3^n W_2^n W_1^n \mathbf{v}^n \end{cases}$$

As mentioned before, since low-level features in all abnormalities are common, the parameters of first layer (primary) of the trained neural networks can be merged (the parts inside the box of Fig. 5, with solid line) to eliminate redundant computations and save memory. As such, suppose

we merge the weights of the first layer (in the box with solid line) of all the n trained networks. In this case, the network of Fig. 6, can be an alternative with significant reduction of memory requirement and computations, and the goal is to design it in such a way that the output of both networks could be the same. For this network, we can assume that the weight matrix of the common primary layer is $W_1 = W_1^j + \Delta W_1^j$ where $1 \leq j \leq n$, so the j th output for input \mathbf{v}^j would be

$$\begin{aligned} \widehat{\mathbf{y}}^j &= W_3^j W_2^j W_1^j \mathbf{v}^j \\ \widehat{\mathbf{y}}^j &= W_3^j W_2^j (W_1^j + \Delta W_1^j) \mathbf{v}^j \\ \widehat{\mathbf{y}}^j &= W_3^j W_2^j W_1^j \mathbf{v}^j + W_3^j W_2^j \Delta W_1^j \mathbf{v}^j \\ \widehat{\mathbf{y}}^j &= \mathbf{y}^j + W_3^j W_2^j \Delta W_1^j \mathbf{v}^j \end{aligned}$$

So in order to have the same output for both networks, i.e. $\widehat{\mathbf{y}}^j = \mathbf{y}^j$ (in element-wise sense), the secondary layers should be retrained.

Now going back to Fig. 4, the primary part of the new network is then followed by two secondary branches of the final network. One of these secondary branches performs the classification task, and the other one is dedicated to the segmentation task. In the segmentation branch of the final network, each secondary sub-network is exclusively trained using a specific abnormality so that it could precisely segment that abnormality. Also in the classification branch of the final network, each secondary sub-network is trained to identify a specific abnormality. Finally, segmentation results are fused with classification results and will make the final classified segmented map. Different parts of Fig. 4, are explained in more details in the following.

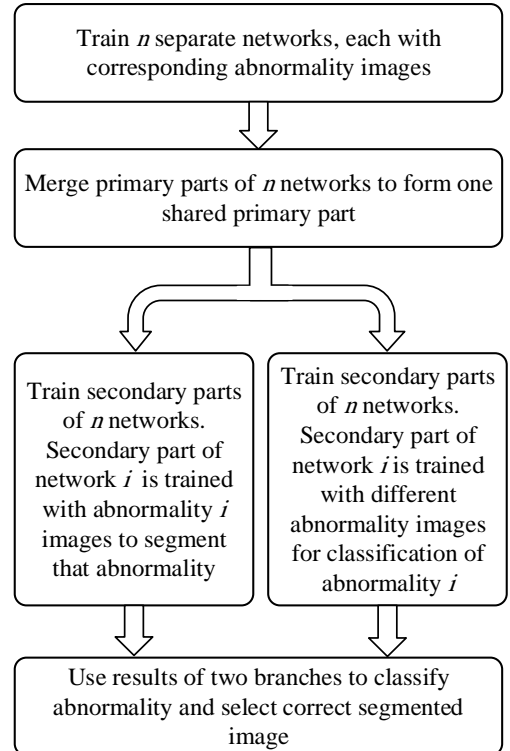


Fig. 4. Main steps of the proposed network formation framework.

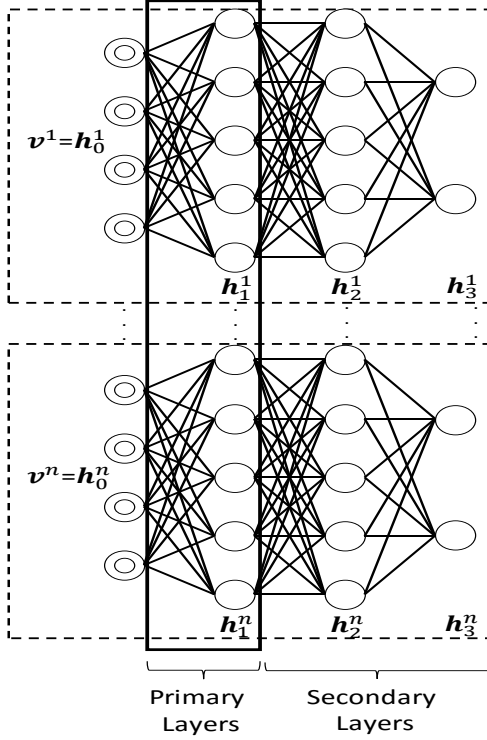


Fig. 5. Neural networks trained on specific class of inputs

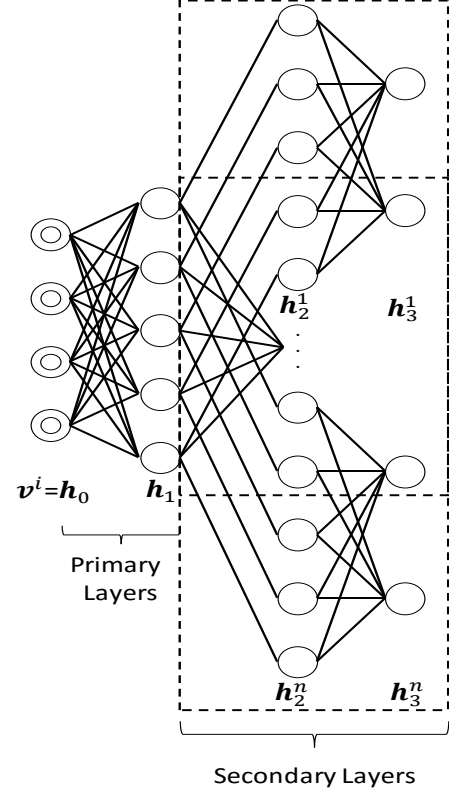


Fig. 6. Merging primary layers of separate neural networks

B. Separate network structure for each abnormality

As it was mentioned in section II-B, a straightforward solution for segmentation can be realized by assigning separate networks to each abnormality. In this way, separate networks are trained on images containing only one abnormality, and each network is responsible for segmentation of the corresponding abnormality's images. In order to evaluate performance of separate network structures for each abnormality, an experiment is conducted using MNIST dataset. MNIST is an image dataset containing 10 classes of English handwritten numbers. 50,000 and 10,000 image samples are used for the network training and testing respectively. As illustrated in Fig. 7a, a separate network is dedicated to each class of numbers. Each network is a CNN structure with 64 and 32 filters in *convolutional layers* (CLs) and with 200 and 100 neurons in *fully connected layers* (FCLs). Each network is responsible to discriminate between its own class and other classes of numbers. In this structure, each network is trained to classify images of its own class as "POSITIVE" and other nine classes as "NEGATIVE". Results of each network are shown in Table I. Although for each class of numbers proper results are obtained, this structure cannot be used for classification of all classes of numbers. To have a network with classification capability, an input image with unknown number's class should be applied on all ten networks and after that a procedure must be considered to vote between results of different networks. In addition to the classification problem, ten separate networks for ten numbers lead to a network with great structural complexity. Generally for medical applications, this approach could lead to complex

structures and redundant operations. Besides, we need to know the type of abnormality before feeding the medical image into

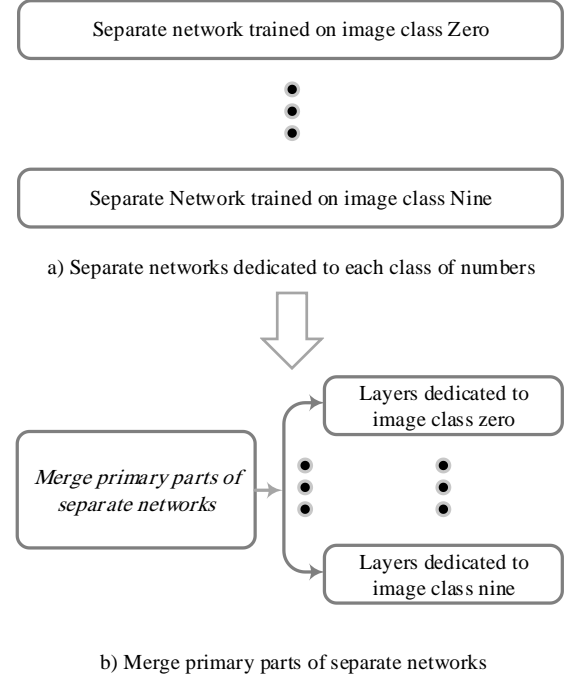


Fig. 7. Training separate network and merging primary parts of separated network on MNIST dataset.

Table. I. Result of separate network structures dedicated to each class of numbers on MNIST dataset

Class of numbers	Accuracy
0	99.94
1	99.90
2	99.86
3	99.90
4	99.89
5	99.87
6	99.82
7	99.77
8	99.89
9	99.69

an appropriate network for segmentation.

C. Merge primary parts of separate networks

There are similarities among all images from multiple abnormalities at least in the normal parts of these images. General features extracted from all images could be assigned to a shared part of the final network. Using a network with a shared part, redundant computations can be eliminated and network structure would be simplified. As illustrated in Fig. 7b, separate networks for each class of numbers in MNIST dataset are merged with each other to share primary parts of their structures with each other. To discriminate between images from different number's classes, a secondary parts is considered for each class of numbers named as class-specific (abnormality-specific) layer to detect number's class. For MNIST dataset, primary part is considered as layers which are two CLs with 64 and 32 filters and secondary parts for each number is considered as FCLs with 200 and 100 neurons. Results of network with shared primary parts (merged network) are illustrated in Table II.

For better comparison, we test a monolithic structure for MNIST dataset as is common in research papers. In the monolithic network a single structure is dedicated for all 10 number's classes and results are illustrated in Table II. Monolithic network is a CNN structure with 64 and 32 filters in CLs and with 200 and 100 neurons in FCLs. As illustrated in Table II, classification accuracy 99.46 and 99.23 are resulted for monolithic and merged network respectively. It can be observed that in case of MNIST classification problem, primary part of the networks for each class of numbers can be merged. Also in the secondary part, separate networks can be considered for each class of numbers. Although in case of classification of MNIST dataset, merging operation does not

lead to increase in performance, but grants classification capability to the separated networks for each number and reduces total network complexity.

In case of medical applications which both classification and segmentation are required, merging operation reduces the number of computational operations significantly. When we look at the merged network for multiple abnormality detection in medical applications, the primary part of merged networks are similar among different abnormalities' network. The primary part is dedicated to the extraction of general features and without merging could be considered as redundant. The secondary part of network which is included abnormality-specific networks is dedicated to each specific abnormality. In the proposed merged network, variables in the primary common part are trained on all abnormalities. Networks in the secondary parts are trained on each abnormality separately. Networks' layers in the primary part can be merged in different ways depending on the variety of abnormalities. In a simple schema, the primary layers of each separate network are designed to have the same neural elements, and their variables can be averaged to make the primary part of the final merged network. In Fig. 8 proposed bifurcated structure for multiple abnormality detection is illustrated. As shown in Fig. 8, the shared primary part is bifurcated into two main branches. One branch is dedicated to abnormality-specific segmentation, and the other branch performs abnormality classification. The primary part of the merged network is once used during the training of the segmentation path of the network and during the training of the classification branch of the bifurcated network. In the next two sub-sections, primary part of the network is used for segmentation and classification respectively.

D. Training the segmentation branch

In the experiment conducted on MNIST, it was observed that primary parts of the separated networks were merged and 10 networks were dedicated to each class of numbers. This experiment shows that there are primary parts in MNIST which are common in all images. Also in order to be able to specify different number's classes, there is an essential need to consider secondary part for each class of numbers. In this section we use merging operation as we conducted in MNIST experiment to make bifurcated network for segmentation and classification.

As illustrated in Fig. 8, the secondary part of the final merged network in segmentation branch consists of multiple sub-networks (named as abnormality-specific layers) dedicated to each abnormality exclusively. The secondary parts of separate networks could make these sub-networks. Primary part of the network is trained on all image abnormalities. Since the primary parts of the separated networks are now merged, the abnormality-specific layers should be re-trained. The abnormality-specific layers are exclusively trained for each abnormality. In this manner, in the final merged network, the shared low-level features are produced in the primary part and high-level specialized features for each abnormality are generated by the abnormality-specific layers located in the secondary part of the network. When an image with abnormality of type "i" is sent to all n segmentation networks,

Table. II. Classification result of different network structures on MNIST image dataset

Network structures	Accuracy
Monolithic	99.46
Merged	99.23

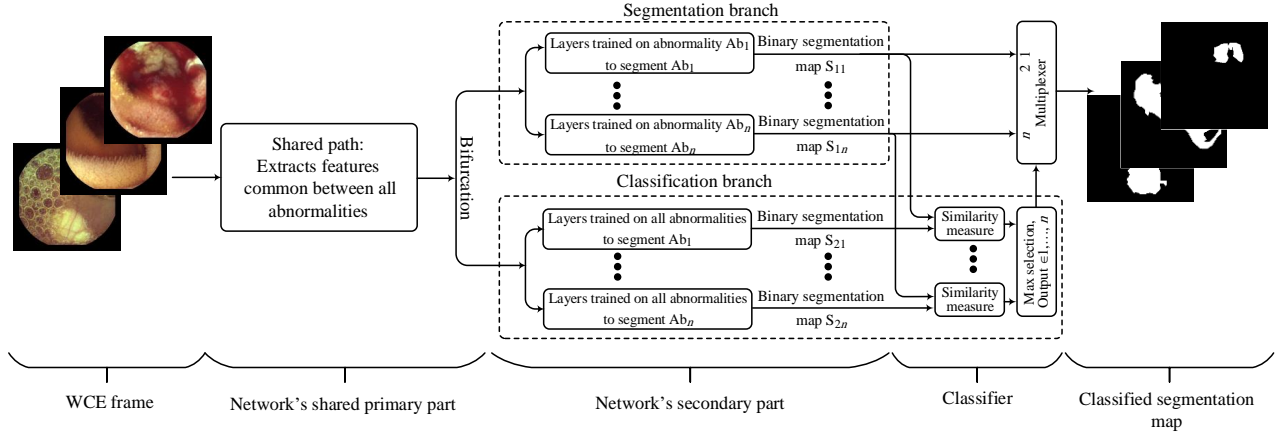


Fig. 8. Proposed bifurcated network structure for multiple-abnormality detection.

only network i is expected to perform accurate segmentation and other segmentation networks have invalid segmentation result for that image. All networks of the segmentation branch produce segmentation maps for abnormality i . The classifying branch will select the output of network i .

E. Training the classification branch of the network

Generally, forming a single network for classification of all abnormalities is either impossible or it can only be achieved by a very complex structure. Hence, we reused the primary part of the final merged network to train another set of abnormality-specific layers for classification as illustrated in Fig. 8. We use all types of abnormality images to train each of these n networks. When a network i sees other abnormality images it considers them as normal. Network i is trained to segment only its own abnormality type. Hence, this type of segmentation contains implied classification.

As illustrated in Fig. 8, the secondary parts of all networks in the classification branch are trained with different abnormalities. The primary part of the network is the same shared primary part of the merged segmentation network. Each abnormality-specific layer in classification branch is dedicated to a specific abnormality but is trained using all abnormalities.

Segmentation branch produces a set S of binary segmentation maps ($S = \{S_1, \dots, S_n\}$). Also the networks in the classification branch produce a set C of binary classification maps ($C = \{C_1, \dots, C_n\}$). We can select the best S_i if we know which type of abnormality is being segmented. We propose that all pairs of binary segmentation maps, $\{S_i, C_i\}_{i \in 1, \dots, n}$, should be compared by calculating their similarities using (1) where " $|\cdot|$ " refers to cardinality operator.

$$\text{similarity}(i) = \left(\frac{|S_i \cap C_i|}{|S_i|} + \frac{|S_i \cap C_i|}{|C_i|} \right) / 2 \quad (1)$$

Those pixels detected as abnormality by either the segmentation branch or the classification branch are represented as 1's in the binary intersection map. The k th pair is selected such that

$$k = \arg \max_j (\text{similarity}(j)) \quad j \in \{1, \dots, n\} \quad (2)$$

The intersection of the two binary maps of S_i and C_i forms a binary "intersection map". The selection of the k th pair of intersection map that has the highest similarity, based on (2), indicates that the image has abnormality k and segmentation map S_k will be selected as the output of the network. When the left operand in the addition operation of (1) is close to 1 it indicates that the two maps are similar to each other and are similar to the map produced in the segmentation branch of the network. When the right addition operation of (1) is close to 1 it shows that the maps are similar with each other and are similar to the map generated by the classification branch of the network. The ratio for the number of ones in the intersection map to the number of ones in the segmentation map demonstrates the correspondence between segmentation and classification with respect to the segmentation. This similarity level is expressed by the left operand of the addition operation of (1). Also, the right operand in the addition operation of (1) demonstrates the correspondence between the segmentation and classification with respect to the classification. The similarity metric defined in equation (1), demonstrates the analogy between the classification and segmentation results. The abnormality which maximizes the similarity between corresponding segmentation and classification results is selected as the abnormality class. After determining the abnormality type, corresponding segmentation is considered as the final segmentation result.

IV. EXPERIMENTAL RESULTS

Proposed network structure for classification and segmentation of multiple abnormalities in medical images is implemented using TensorFlow framework. A PC equipped with an Intel(R) Core(TM) i7-4790 CPU 4.00 GHz and 32GB of RAM and NVIDIA GeForce GTX TITAN X is used for the training phase and testing the network performance. Bifurcation approach reduces the number of operations and simplifies network structure and is suitable for applications which require simple operations. Hence, two applications including WCE abnormality and dermoscopic skin lesion detection are experimented. Multiple abnormality segmentation and classification in WCE and dermoscopic images are very useful for better diagnosis and to reduce time

spent by physician for diagnosis. Capsule endoscopy is a tiny device with limited hardware resources and wireless dermatoscope is a battery operated portable device. We are going to have a simple and efficient structure suitable for implementation inside these devices. Hence it is tried to implement a simple network structure and reuse of operations as bifurcation. Bifurcation approach is implemented as one network structure which is trained and tested on the WCE abnormality image. KID and bleeding data set are considered and images including bleeding, angioectasias, chylous and lymphangiectasia are used from [46] and [47]. Images used for training and testing of WCE, include 50 bleeding, 27 angioectasias, 8 chylous and 9 lymphangiectasias images. For better evaluation, bifurcation approach is implemented as another network structure which is trained and tested on the skin lesion image data set (PH2) including common nevus, atypical nevus and melanoma which is publicly available at [48]. PH2 includes 80 common nevus, 80 atypical nevus and 40 melanoma images.

We used accuracy, sensitivity and specificity for evaluation of classification and segmentation. In order to better evaluate segmentation results, we used DICE score which is an appropriate metric in case of the dataset with imbalance data problem. Overlapping image patches and their central pixels are used as network's input and desired label, respectively during the training process. WCE input images are converted to three different color channels including gray-scale level, "S" channel of HSV color space, and 'a' channel of CIE-lab color space and RGB channels are used for PH2 images. For each of the three different channels, patches with the size of 9×9 are selected as network inputs, and the central pixel is labeled according to the corresponding ground truth. Training data is balanced in such a way that the number of healthy patches is twice the number of abnormal patches. Simulation results are organized in the following subsections.

A. Single network structure for classification of all abnormalities

Two single structures of the convolutional neural network is applied for classification of abnormalities in WCE and dermoscopic images. Different single structures were tested with different convolutional and fully connected layers, and the best one is selected. The best network has two CLs with 64 and 32 kernels as well as two FCLs with 60 and 40 neurons. Classification is performed for each pixel based on patch-wise approach, and visual results of six WCE and dermoscopic images containing different abnormalities are illustrated in Fig. 9 and Fig. 10, respectively. In Fig. 9, classification results of bleeding, angioectasias, chylous and lymphangiectasia are colored with red, yellow, green and blue respectively. Also in Fig. 10, classification results of common nevus, atypical nevus and melanoma are colored with green, blue and red respectively. Visual results of classifications show that single network structure is not able to properly classify the abnormalities. In images in Fig. 9 and Fig. 10, some regions are wrongly classified. Although the single network is not able to distinguish different abnormality classes, the abnormal parts of the corresponding abnormality are segmented approximately. For example in images with angioectasias abnormality in Fig. 9, angioectasias parts are almost colored yellow correctly. Also in common nevus images of Fig. 10, common nevus lesion parts are almost colored green correctly. Although there are other colored regions in the result of segmentation, regions with the correct abnormality are similar to the ground truth approximately.

B. Separate network structures for each abnormality

Separate network structures dedicated to each abnormality are set up for segmentation task. Since the primary parts of these networks will be merged into each other during the next steps, these parts are selected to have the same configuration in primary part.

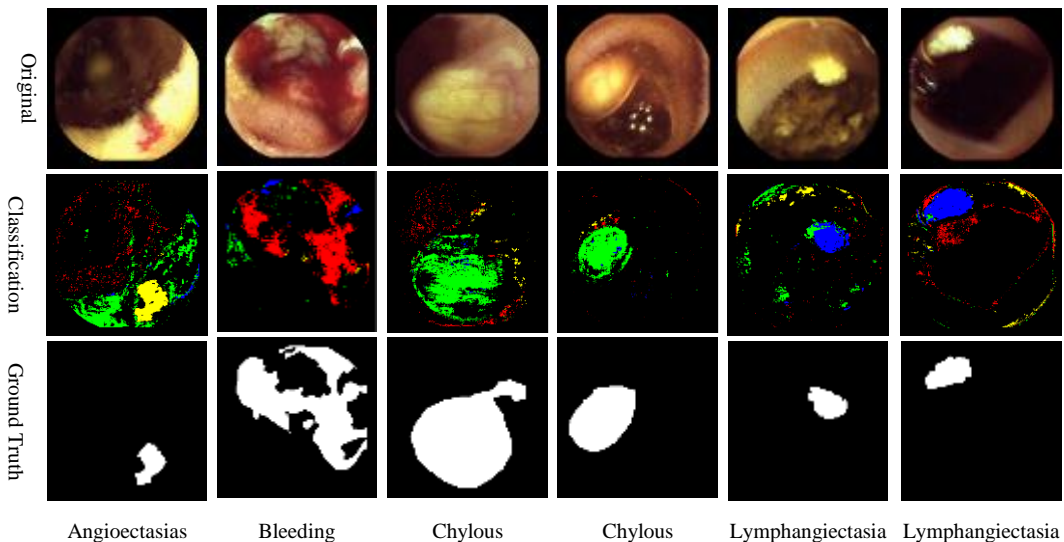


Fig. 9. Visual results of the single classification network for WCE images

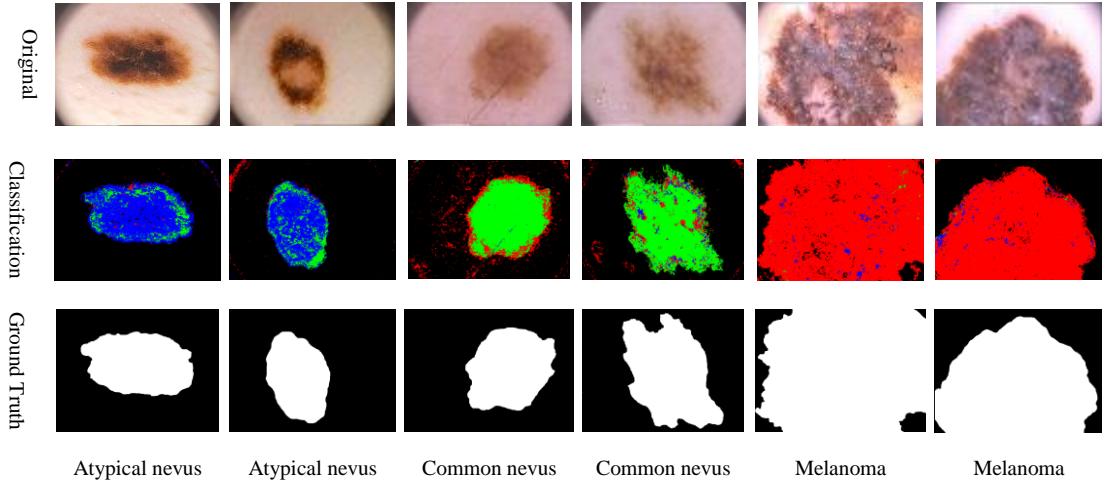


Fig. 10. Visual results of the single classification network for dermoscopic images

For WCE, four networks which have two CLs with 64 and 32 convolutional filters and two FCLs with hidden layers containing 60 and 40 neurons are trained with a set of images containing only one abnormality. Also for dermoscopic images, three networks which have two CLs with 64 and 32 convolutional filters and two FCLs with two hidden layers containing 60 and 40 neurons are trained with a set of images containing only one abnormality. For evaluation of each separate network, segmentation is performed only on images of corresponding abnormality. Visual results on sample WCE and skin lesion images are illustrated in Fig. 11 and Fig 12 respectively. Segmentation results represent that proper segmentation is obtained using separate networks dedicated to each abnormality. Dice score and accuracy of each segmented abnormality are provided in Table III and Table IV. Since each network is trained on a special abnormality, it is not able to discriminate between different abnormality classes. Although acceptable segmentation results are obtained, this structure is not able to classify the images into proper classes.

C. Separate networks with merged primary parts

As merging primary layers of separate networks reduces computational operations and simplifies the network's structure, we merged the convolutional layers of all separate networks to make a new segmentation network with the merged primary layer. Then we trained primary part of merged network as common layers and trained secondary part as abnormality-specific layers for each abnormality. For WCE and skin lesion images four and three abnormality-specific layers are considered respectively. Abnormality-specific layers in WCE and skin lesion networks have two FCLs with 60 and 40 neurons. Quantitative results of the segmentation network with merged primary part for WCE and skin lesion image dataset are illustrated in Table V and Table VI respectively. Table V and VI, indicate that there is no significant difference from the previous separate networks' results in Table III and Table IV respectively. As it was observed in MNIST experiment, merging primary part of separate network reduces network complexity with no significant loss of network performance.

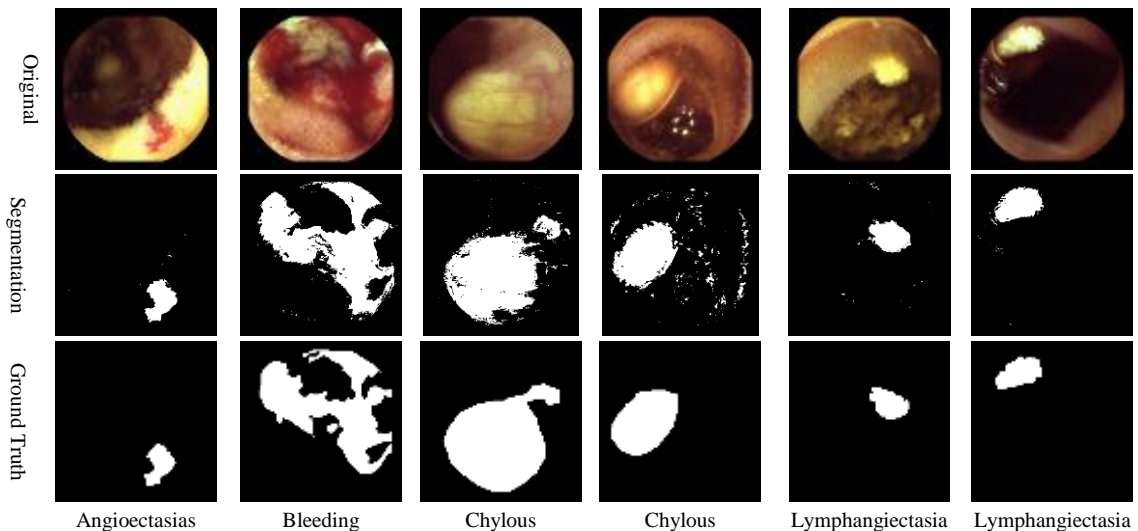


Fig. 11. Visual results of the segmentation with separate networks for WCE images

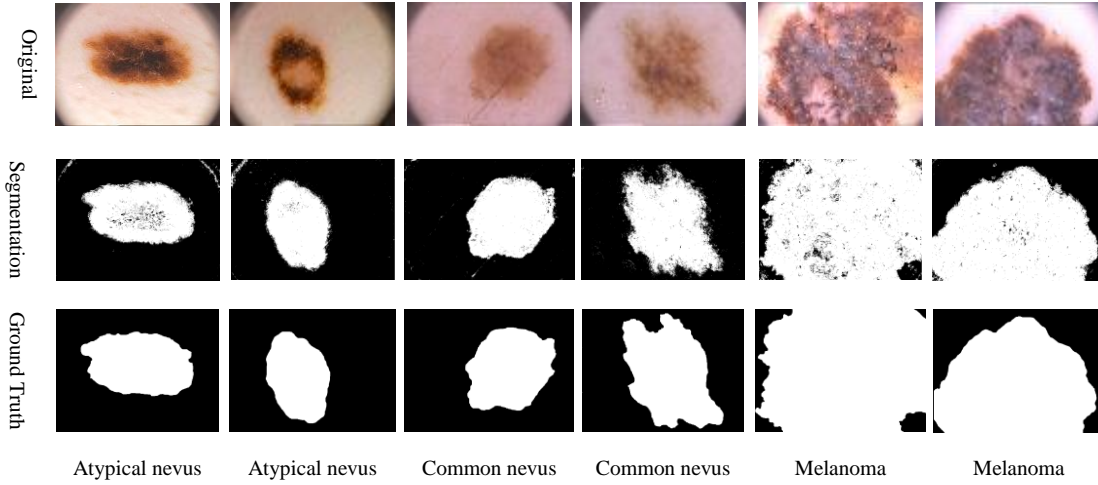


Fig. 12. Visual results of the segmentation with separate networks for dermoscopic images

In the problem of multiple abnormality detection in medical applications, we employed the primary parts in another direction for classification task.

D. Bifurcated network for classification and segmentation

Network structure in the previous section has a primary and secondary part used for segmentation. As illustrated in Fig. 8, the primary part of this network is used in another path for the classification task, and a secondary part is also considered for classification. For WCE and skin lesion images, four and three abnormality-specific layers are considered respectively. Abnormality-specific layers in WCE and skin lesion networks have two FCLs with 60 and 40 neurons. In Fig. 13 and Fig. 14, classification results in case of six WCE and six dermoscopic image samples are illustrated respectively. Due to assigning abnormality-specific layers for each abnormality, in Fig. 13, four outputs are indicating the correspondence between image pixels and WCE abnormality classes. Also in Fig. 14, three outputs are indicating the correspondence between image pixels and skin lesion classes.

It can be observed from Fig. 13 and Fig. 14, that classification results in related classes are close to the image ground truth. For example results of chylous images in part of chylous classes are much similar to the ground truth than the others. In this step the applied network for classification is not similar to the experimented monolithic network. We should indicate that the monolithic network used in section IV-A which can segment all abnormalities has a highly complex structure as compared to the proposed bifurcated network. Also, segmentation map resulted from monolithic network is not accurate as result of separate network for each abnormality.

The network still is not able to decide between abnormality classes. Also as it was observed in Fig. 10, segmentation results are similarly proper but the network is not able to decide between different abnormality classes. Classified results of the merged bifurcated network are used to obtain the final classified-segmented results. In Fig. 11 and Fig. 13 for WCE images as well as Fig. 12 and Fig. 14, for dermoscopic images, it was observed that results of corresponding

segmentation and classification are similar in their own abnormalities. For example for an angioectasias image in Fig. 13, the classification result in the angioectasias class is similar to the segmentation result of the corresponding image in Fig. 11. Also melanoma lesion segmentation result in Fig. 12, is similar to the result of melanoma class in Fig. 14. Hence using equation (1), abnormality-specific layer with maximum similarity is selected as the class of the abnormality.

Table III. Quantitative results of segmentation using dedicated network for each WCE abnormality

Abnormality	Accuracy	DICE
Angioectasias	0.99	0.76
Bleeding	0.94	0.86
Chylous	0.96	0.86
Lymphangiectasia	0.99	0.94

Table IV. Quantitative results of segmentation using dedicated network for each skin image abnormality

Abnormality	Accuracy	DICE
Common nevus	0.973	0.940
Atypical nevus	0.960	0.930
Melanoma	0.951	0.962

Table V. Quantitative results of segmentation using merged network for all WCE image abnormalities

Abnormality	Accuracy	DICE
Angioectasias	0.99	0.76
Bleeding	0.91	0.85
Chylous	0.95	0.85
Lymphangiectasia	0.99	0.93

Table VI. Quantitative results of segmentation using merged network for all skin image abnormalities

Abnormality	Accuracy	DICE
Common nevus	0.972	0.939
Atypical nevus	0.956	0.922
Melanoma	0.944	0.957

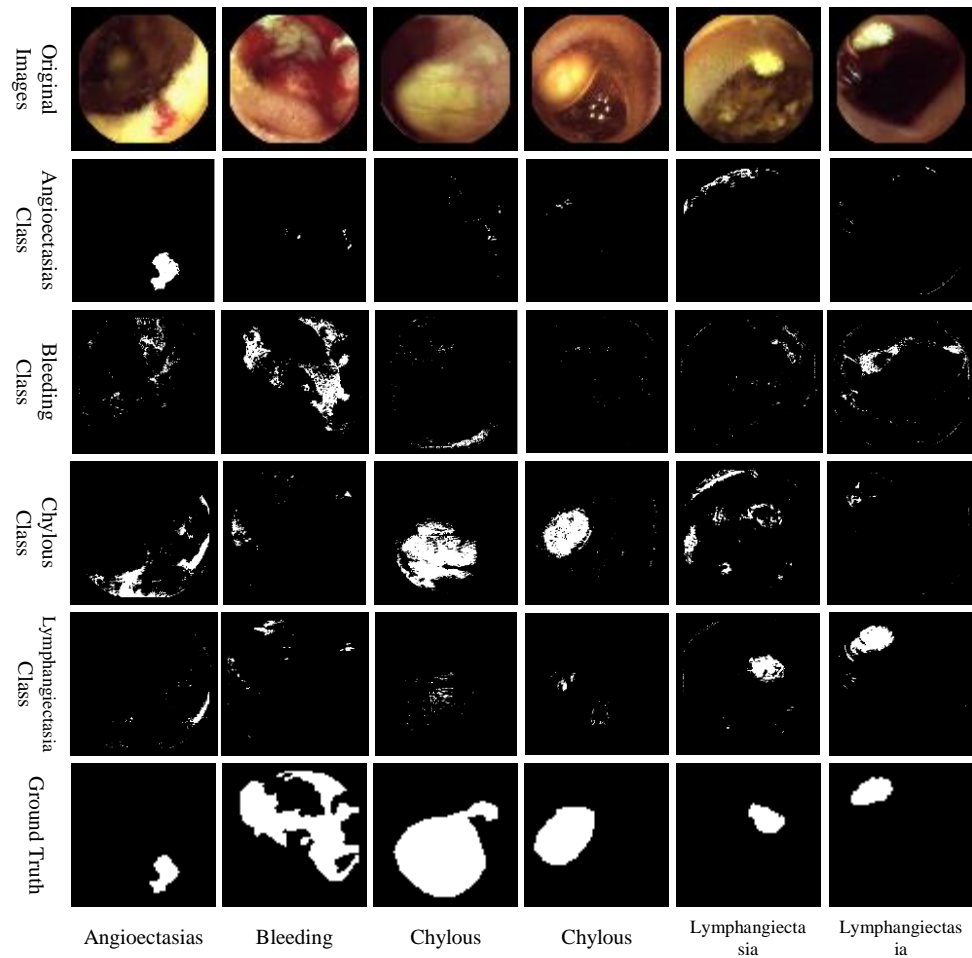


Fig. 13. Results of the classification network with merged primary part for WCE images

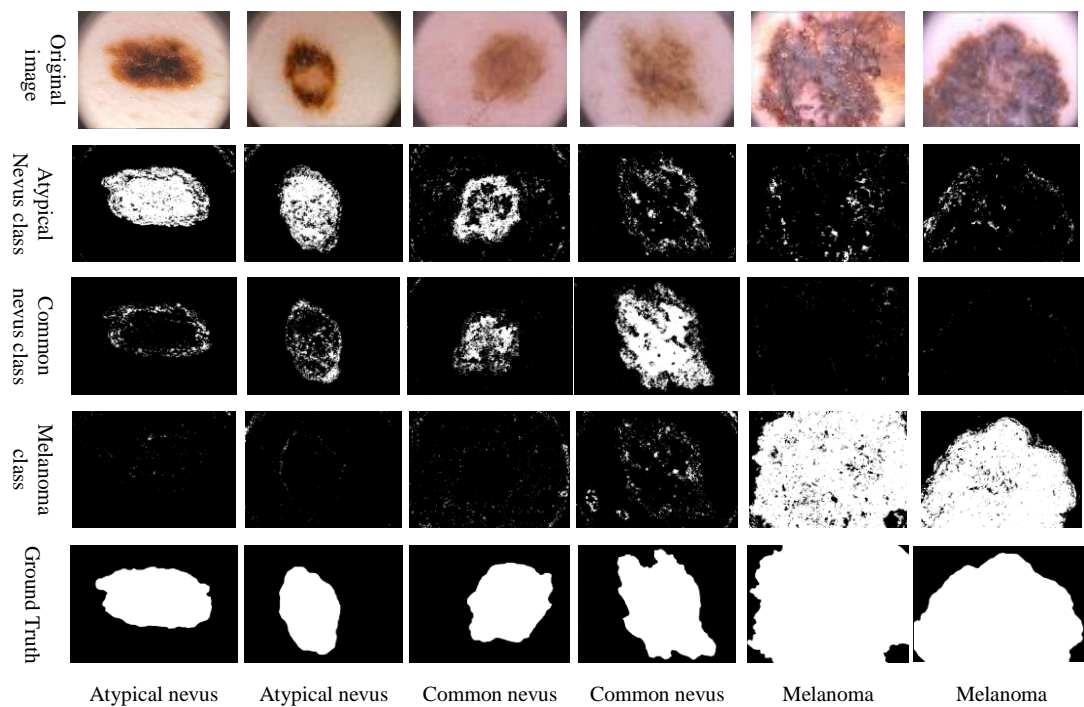


Fig. 14. Results of the classification network with merged primary part for dermoscopic images

In Fig. 15 and Fig. 16, visual results of the bifurcated network in case of sample WCE and dermoscopic images are shown respectively. According to our observations, proper classification and segmentation are possible by using the fused results of segmentation and classification directions. Using fused result of bifurcated network, selection of the best segmentation results from segmentation branch is realized. Also, fused result help to classify input image properly. In Table VII and VIII, the number of true and false predictions of abnormality classes in WCE and dermoscopic image dataset is shown respectively. Only one abnormal image that belongs to angioectasias class is misclassified as Lymphangiectasia. Also one melanoma image is wrongly classified as other classes and one image from other classes are misclassified as melanoma. Proper classification results from Table VII and VIII, realized using fused results of segmentation and classification.

In Fig. 17 binary maps produced from intersection of segmentation and classification maps for a sample bleeding image are illustrated. Binary segmentation and classification maps correspond to each abnormality-specific layer are presented in top and bottom row of Fig 17, respectively. In the middle row of Fig. 17, intersection of segmentation and classification maps indicates similarity between these two maps in the corresponding abnormality. It can be observed that the intersection results in the bleeding part are similar to both the corresponding segmentation and classification map.

In practical experiments employing only classification map may not lead to appropriate results and to achieve better classification using intersection map is necessary. Using equation (1), the abnormality correspond to the most similar intersection map is regarded as detected abnormality class.

In Table IX and X, quantitative results of the proposed bifurcated network for WCE abnormality and skin lesion detection are compared with related works respectively. In Table IX, Table X, relative abnormality detection methods have used various features as well as post-processing procedures. However the proposed method does not use any features and only biggest connected component is used as post-processing procedure. In Table IX, Different abnormalities are investigated based on different methods on the WCE images. In [5] maximum posterior (MAP) as well as Markov random field (MRF) are used to segment angioectasias images. In [6], [13] and [14], SVM is utilized for segmentation of bleeding and angioectasias images. In [7] and [8], bleeding WCE images are segmented using SVM. Also in [39], ANN is used for segmentation of bleeding images. In [9] and [15] different types of abnormalities including chylous, bleeding and Lymphangiectasia are classified in image level. The proposed method results are close to the results of the previous methods for all abnormalities. In [9] and [15] the results are image based classification and segmentation is not conducted. Our

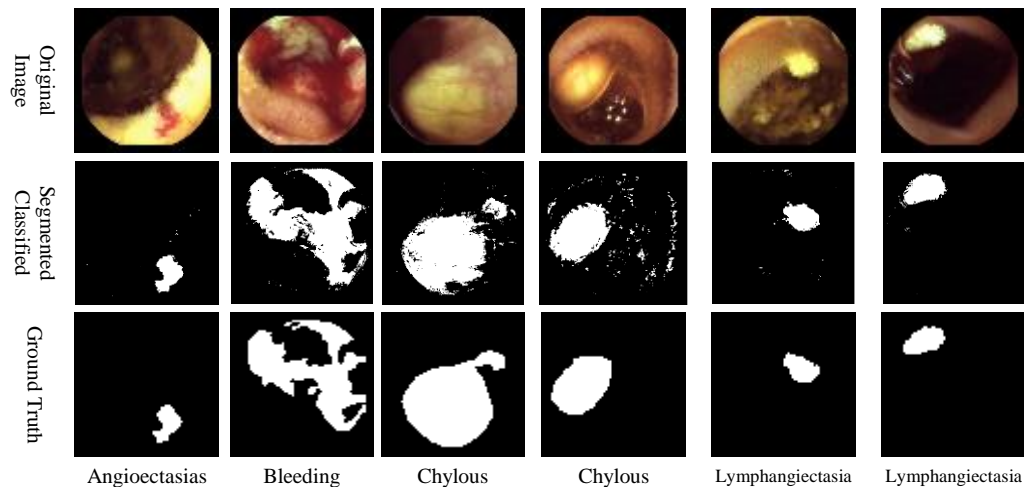


Fig. 15. Final classified-segmented results for WCE images

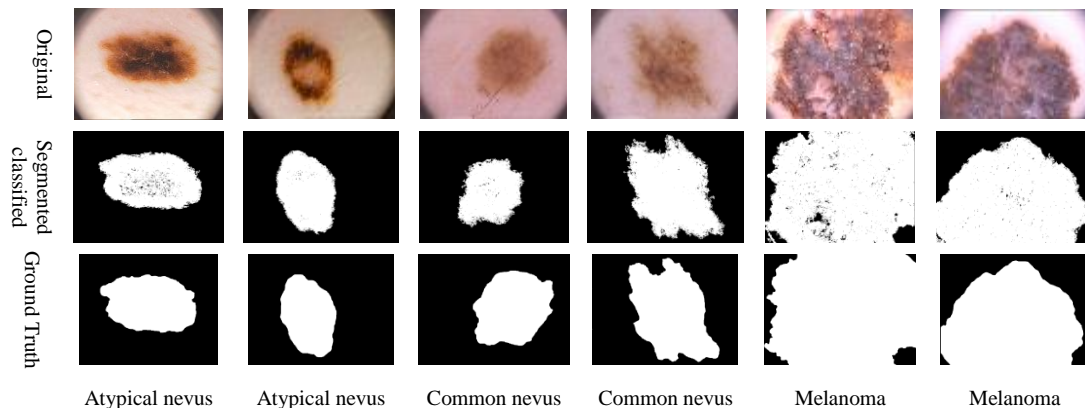


Fig. 16. Final classified-segmented results for dermoscopic images

proposed network is able to effectively classify abnormality in image level and in Table VII, only one misclassification is observed. For better evaluation of the proposed method, also results of single CNN structure for segmentation is reported in

Table VII. Number of true and false predictions of WCE abnormality classes

	Angioectasias	Bleeding	Chylous	Lymphangiectasia
Angioectasias	26	0	0	1
Bleeding	0	50	0	0
Chylous	0	0	8	0
Lymphangiectasia	0	0	0	9

Table IX. It can be observed in Table IX, that the results of the proposed method are better than our single CNN except for angioectasias that similar Dice is obtained. It is important to note that the proposed network can classify and segment different types of abnormalities.

Table VIII. Number of true and false predictions of skin lesion classes in PH2 dataset

	Atypical nevus	Common nevus	Melanoma
Atypical nevus	72	8	1
Common nevus	3	77	0
Melanoma	1	0	39

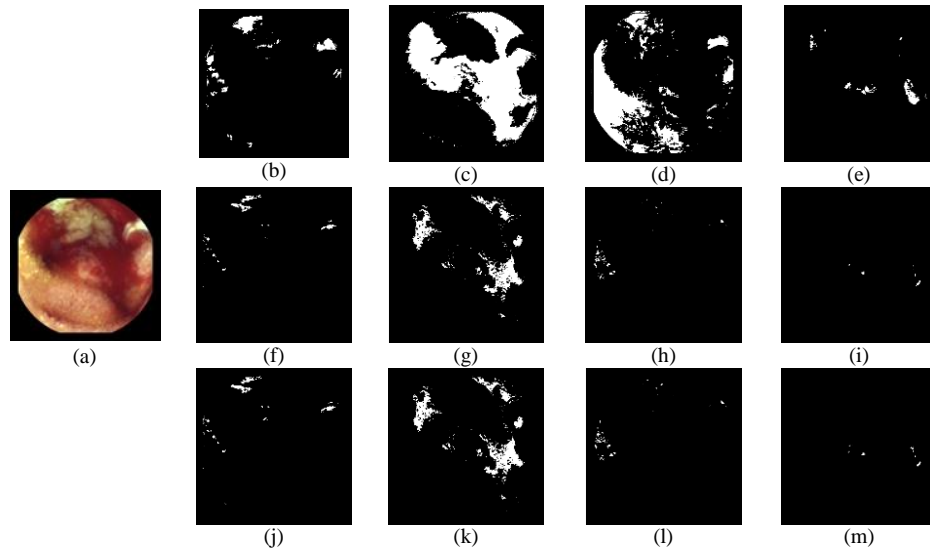


Fig. 17. Binary maps produced from intersection of segmentation and classification maps for a sample input image. (a) input image, (b), (c), (d), (e) binary maps from lymphangiectasia, bleeding, Chylous, and angioectasias networks of the segmentation branch, (f), (g), (h), (i) intersection maps, (j), (k), (l), (m) binary maps from lymphangiectasia, bleeding, Chylous, and angioectasias networks of the classification branch.

Table IX. Comparative results of the proposed method on WCE images with related works

	Angioectasias	Bleeding + Angioectasias	Bleeding	Chylous	Lymphangiectasia
MAP+MRF [5]	DICE : 0.76	--	--	--	--
SVM [13]	--	Sen: 0.91 Spec : 0.96	--	--	--
SVM [6]	--	Sen: 0.88 Spec : 0.84	--	--	--
SVM [14]	--	Sen : 0.78 Spec : 0.99	--	--	--
SVM [8]	--	--	DICE: 0.84	--	--
SVM [7]	--	--	DICE: 0.81	--	--
ANN [39]	--	--	DICE: 0.85	--	--
SVM [9]	--	--	AUC: 0.83	AUC : 0.87	AUC: 0.96
CNN [15]	--	--	AUC: 0.64	AUC : 0.87	AUC : 0.95
Monolithic CNN	DICE: 0.76	Sen : 0.46 Spec: 0.99	DICE: 0.52	DICE: 0.74	DICE: 0.91
Proposed	DICE: 0.76	Sen: 0.81 Spec: 0.99	DICE: 0.85	DICE: 0.85	DICE: 0.93

Table X. Comparative results of the proposed method on dermoscopic images with related works

	Classification			Segmentation			
	Sen	Spe	Acc	Sen	Spe	Acc	Dice
[20], ANN	0.957	100	0.967	--	--	--	--
[21], KNN	0.960	0.830	--	--	--	--	--
[22], SVM	0.977	0.967	0.975	--	--	--	--
[24], FCN	--	--	--	--	--	--	0.938
[25], FCN	--	--	--	0.948	0.939	0.942	0.906
[26], SVM & RF	100	0.882	--	--	--	--	--
[27], region growing	--	--	--	0.876	0.953	0.934	--
[28], SVM	0.96	0.97	--	--	--	--	--
[29], SVM	0.950	0.950	0.950	95.4	0.981	0.965	0.920
[30], Delaunay Triangulation	--	--	--	0.802	0.972	0.896	--
Monolithic, CNN	--	--	--	0.724	0.978	0.891	0.820
Proposed, CNN	0.975	0.993	0.990	0.924	0.978	0.960	0.940

In Table X, [20], [21], [22], [26], [28] and [29], classified skin lesions in malignant and non-malignant classes and in [24], [25], [27], [29] and [30], skin lesion segmentation is investigated. Although in some research studies both segmentation and classification are conducted but only in [29], results of segmentation and classification are reported. In comparison with [29], better classification results are obtained. Also Dice score in segmentation is better and similar accuracy and specificity are observed. In Table X, Dice score 0.82 is observed for segmentation in single CNN structure while proposed bifurcated network has Dice score 0.94. In comparison with other related work in Table X, in the proposed framework, segmentation and classification tasks are investigated but in both tasks, acceptable results are observed. Finally it can be noted that, using fused results of two branches including segmentation and classification taken from a primary network layers, both segmentation and classification is obtained effectively.

V. CONCLUSION

A simple neural network structure was designed for classification and segmentation of multiple abnormalities for portable medical instruments. The proposed bifurcated network was equipped with a primary part to extract the common features and two secondary parts for classification and segmentation. Secondary parts could be specialized for each abnormality to achieve better results. Since the proposed structure was designed to be used inside the portable device, it was designed to be simple and benefit from the shared parts of operations. Simulation results were conducted in case of multiple abnormalities in two medical portable applications including WCE and dermoscopy. It was observed that the proposed network was able to segment and classify WCE and dermoscopic images simultaneously. Also utilizing primary parts of the network prevented redundant operations which make it suitable for implementation inside the portable medical devices.

REFERENCES

- [1] M. Keroack, *Video capsule endoscopy*, vol. 20, no. 5. 2004.
- [2] D. K. Iakovidis and A. Koulaouzidis, "Software for enhanced video capsule endoscopy: Challenges for essential progress," *Nat. Rev. Gastroenterol. Hepatol.*, vol. 12, no. 3, pp. 172–186, 2015.
- [3] X. Jia and M. Q.-H. Meng, "A deep convolutional neural network for bleeding detection in Wireless Capsule Endoscopy images," *2016 38th Annu. Int. Conf. IEEE Eng. Med. Biol. Soc.*, pp. 639–642, 2016.
- [4] X. Jia and M. Q. H. Meng, "Gastrointestinal bleeding detection in wireless capsule endoscopy images using handcrafted and CNN features," *Proc. Annu. Int. Conf. IEEE Eng. Med. Biol. Soc. EMBS*, pp. 3154–3157, 2017.
- [5] P. M. Vieira, B. Goncalves, C. R. Goncalves, and C. S. Lima, "Segmentation of angiodysplasia lesions in WCE images using a MAP approach with Markov Random Fields," *Proc. Annu. Int. Conf. IEEE Eng. Med. Biol. Soc. EMBS*, vol. 2016–Octob, pp. 1184–1187, 2016.
- [6] Y. Fu, W. Zhang, M. Mandal, and M. Q. H. Meng, "Computer-aided bleeding detection in WCE video," *IEEE J. Biomed. Heal. Informatics*, vol. 18, no. 2, pp. 636–642, 2014.
- [7] F. Deeba, F. M. Bui, and K. A. Wahid, "Automated Growcut for segmentation of endoscopic images," *Proc. Int. Jt. Conf. Neural Networks*, vol. 2016–Octob, pp. 4650–4657, 2016.
- [8] E. Tuba, M. Tuba, and R. Jovanovic, "An algorithm for automated segmentation for bleeding detection in endoscopic images," *Proc. Int. Jt. Conf. Neural Networks*, vol. 2017–May, pp. 4579–4586, 2017.
- [9] D. K. Iakovidis and A. Koulaouzidis, "Automatic lesion detection in wireless capsule endoscopy - A simple solution for a complex problem," *Image Process. (ICIP), 2014 IEEE Int. Conf. on. IEEE*, pp. 2236–2240, 2014.
- [10] S. Seguí, M. Drozdal, G. Pascual, P. Radeva, C. Malagelada, F. Azpiroz, and J. Vitrià, "Generic feature learning for wireless capsule endoscopy analysis," *Comput. Biol. Med.*, vol. 79, no. July, pp. 163–172, 2016.
- [11] Y. Yuan, X. Yao, J. Han, L. Guo, and M. Q. H. Meng, "Discriminative Joint-Feature Topic Model With Dual Constraints for WCE Classification," *IEEE Trans. Cybern.*, pp. 1–12, 2017.
- [12] Y. Zou, L. Li, Y. Wang, J. Yu, Y. Li, and W. J. Deng, "Classifying Digestive Organs in Wireless Capsule Endoscopy Images Based on Deep Convolutional Neural Network," pp. 1274–1278, 2015.
- [13] D. K. Iakovidis, D. Chatzis, P. Chrysanthopoulos, and A. Koulaouzidis, "Blood detection in wireless capsule endoscope images based on salient superpixels," *Proc. Annu. Int. Conf. IEEE Eng. Med. Biol. Soc. EMBS*, vol. 2015–Novem, no. 1, pp. 731–734, 2015.

- 2015.
- [14] D. K. Iakovidis and A. Koulaouzidis, "Automatic lesion detection in capsule endoscopy based on color saliency: Closer to an essential adjunct for reviewing software," *Gastrointest. Endosc.*, vol. 80, no. 5, pp. 877–883, 2014.
- [15] A. K. Sekuboyina, S. T. Devarakonda, and C. S. Seelamantula, "A convolutional neural network approach for abnormality detection in Wireless Capsule Endoscopy," *2017 IEEE 14th Int. Symp. Biomed. Imaging (ISBI 2017)*, pp. 1057–1060, 2017.
- [16] F. Deebea, S. K. Mohammed, F. M. Bui, and K. A. Wahid, "Unsupervised abnormality detection using saliency and Retinex based color enhancement," *Proc. Annu. Int. Conf. IEEE Eng. Med. Biol. Soc. EMBS*, vol. 2016–Octob, pp. 3871–3874, 2016.
- [17] M. Vasilakakis, D. K. Iakovidis, E. Spyrou, and A. Koulaouzidis, "Weakly-Supervised Lesion Detection in Video Capsule Endoscopy Based on a Bag-of-Colour Features Model," *Int. Work. Comput. Robot. Endosc.*, pp. 96–103, 2016.
- [18] M. D. Vasilakakis, D. K. Iakovidis, E. Spyrou, D. Chatzis, and A. Koulaouzidis, "Beyond lesion detection: Towards semantic interpretation of endoscopy videos," in *Communications in Computer and Information Science*, 2017, vol. 744, pp. 379–390.
- [19] R. Johr and W. Stolz, *Dermoscopy: An Illustrated Self Assessment Guide*. McGraw-Hill Medical Pub., 2010.
- [20] S. Pathan, K. G. Prabhu, and P. C. Siddalingaswamy, "A methodological approach to classify typical and atypical pigment network patterns for melanoma diagnosis," *Biomed. Signal Process. Control*, 2018.
- [21] M. Ruela, C. Barata, J. S. Marques, and J. Rozeira, "A system for the detection of melanomas in dermoscopy images using shape and symmetry features," *Comput. Methods Biomech. Biomed. Eng. Imaging Vis.*, 2017.
- [22] M. Nasir, M. Attique Khan, M. Sharif, I. U. Lali, T. Saba, and T. Iqbal, "An improved strategy for skin lesion detection and classification using uniform segmentation and feature selection based approach," *Microsc. Res. Tech.*, 2018.
- [23] P. P. Rebouças Filho, S. A. Peixoto, R. V. M. da Nóbrega, D. J. Hemanth, A. G. Medeiros, A. K. Sangaiah, and V. H. C. de Albuquerque, "Automatic histologically-closer classification of skin lesions," *Comput. Med. Imaging Graph.*, 2018.
- [24] Y. Yuan, M. Chao, and Y.-C. Lo, "Automatic Skin Lesion Segmentation Using Deep Fully Convolutional Networks with Jaccard Distance," *IEEE Trans. Med. Imaging*, 2017.
- [25] L. Bi, J. Kim, E. Ahn, A. Kumar, M. Fulham, and D. Feng, "Dermoscopic Image Segmentation via Multistage Fully Convolutional Networks," *IEEE Trans. Biomed. Eng.*, 2017.
- [26] C. Barata, M. Emre Celebi, and J. S. Marques, "Development of a clinically oriented system for melanoma diagnosis," *Pattern Recognit.*, 2017.
- [27] S. Pathan, K. G. Prabhu, and P. C. Siddalingaswamy, "Hair detection and lesion segmentation in dermoscopic images using domain knowledge," *Med. Biol. Eng. Comput.*, pp. 1–15, 2018.
- [28] T. Y. Satheesha, D. Satyanarayana, M. N. G. Prasad, and K. D. Dhruve, "Melanoma Is Skin Deep: A 3D Reconstruction Technique for Computerized Dermoscopic Skin Lesion Classification," *IEEE J. Transl. Eng. Heal. Med.*, 2017.
- [29] N. Z. Tajeddin and B. M. Asl, "Melanoma Recognition in Dermoscopy Images Using Lesion's Peripheral Region Information," *Comput. Methods Programs Biomed.*, 2018.
- [30] A. Pennisi, D. D. Bloisi, D. Nardi, A. R. Giampetruzzi, C. Mondino, and A. Facchiano, "Skin lesion image segmentation using Delaunay Triangulation for melanoma detection," *Comput. Med. Imaging Graph.*, 2016.
- [31] A. Rasooly and K. E. Herold, *Mobile health technologies*. Springer, 2015.
- [32] T.-T. Do, T. Hoang, V. Pomponiu, Y. Zhou, C. Zhao, N.-M. Cheung, D. Koh, A. Tan, and T. Hoon, "Accessible Melanoma Detection using Smartphones and Mobile Image Analysis," *IEEE Trans. Multimed.*, 2018.
- [33] P. Sahu, D. Yu, and H. Qin, "Apply lightweight deep learning on internet of things for low-cost and easy-to-access skin cancer detection," in *Medical Imaging 2018: Imaging Informatics for Healthcare, Research, and Applications*, 2018, vol. 10579, p. 1057912.
- [34] G. Zouridakis, X. Yuan, J. Chen, E. Stotzer, and Y. Wu, "Device and software for screening the skin." Google Patents, 03-Jul-2012.
- [35] Y. Wu, J. Chen, X. Yuan, and G. Zouridakis, "A programmable DSP development platform for automated detection of melanoma," *Int. J. Intell. Comput. Med. Sci. Image Process.*, vol. 3, no. 1, pp. 1–8, 2009.
- [36] S. Conoci, F. Rundo, S. Petralta, and S. Battiato, "Advanced skin lesion discrimination pipeline for early melanoma cancer diagnosis towards PoC devices," in *2017 European Conference on Circuit Theory and Design, ECCTD 2017*, 2017.
- [37] I. Mehmood, M. Sajjad, and S. W. Baik, "Video summarization based tele-endoscopy: A service to efficiently manage visual data generated during wireless capsule endoscopy procedure," *J. Med. Syst.*, vol. 38, no. 9, 2014.
- [38] M. A. Khorsandi, N. Karimi, S. Samavi, M. Hajabdollahi, S. M. R. Soroushmehr, K. Ward, and K. Najarian, "Hardware Image Assessment for Wireless Endoscopy Capsules," pp. 2050–2053, 2016.
- [39] M. Hajabdollahi, R. Esfandiarpour, S. M. R. Soroushmehr, N. Karimi, S. Samavi, and K. Najarian, "Segmentation of Bleeding Regions in Wireless Capsule Endoscopy Images: An Approach for inside Capsule Video Summarization."
- [40] P. Turcza and M. Duplaga, "Hardware-Efficient Low-Power Image Processing System for Wireless Capsule Endoscopy," *Biomed. Heal. Informatics, IEEE J.*, vol. 17, no. 6, pp. 1046–1056, 2013.
- [41] P. Turcza and M. Duplaga, "Sensors and Actuators A: Physical Low power FPGA-based image processing core for wireless capsule endoscopy," *Sensors Actuators A. Phys.*, vol. 172, no. 2, pp. 552–560, 2011.
- [42] N. Jarray, "Low complexity and efficient architecture of 1D-DCT based Cordic-Loeffler for Wireless Endoscopy Capsule," pp. 1–5, 2015.
- [43] T. H. Khan, S. Member, and K. A. Wahid, "Low Power and Low Complexity Compressor for Video Capsule Endoscopy," vol. 21, no. 10, pp. 1534–1546, 2011.
- [44] J. H. Tan, U. R. Acharya, S. V. Bhandary, K. C. Chua, and S. Sivaprasad, "Segmentation of optic disc, fovea and retinal vasculature using a single convolutional neural network," *J. Comput. Sci.*, vol. 20, pp. 70–79, 2017.
- [45] J. H. Tan, H. Fujita, S. Sivaprasad, S. V. Bhandary, A. K. Rao, K. C. Chua, and U. R. Acharya, "Automated segmentation of exudates, haemorrhages, microaneurysms using single convolutional neural network," *Inf. Sci. (Ny)*, vol. 420, pp. 66–76, 2017.
- [46] A. Koulaouzidis, "KID: Koulaouzidis-Iakovidis database for capsule endoscopy," 2016.
- [47] F. Deebea, "Bleeding images and corresponding ground truth of CE images," 2016. Available online at <https://sites.google.com/site/farahdeeba073/Research/resources>, accessed on March 2017.
- [48] T. Mendonça, P. M. Ferreira, J. S. Marques, A. R. S. Marcal, and J. Rozeira, "PH 2-A dermoscopic image database for research and benchmarking," in *Engineering in Medicine and Biology Society (EMBC), 2013 35th Annual International Conference of the IEEE*, 2013, pp. 5437–5440.